

Evolution of long-lived globular cluster stars

I. Grid of stellar models with helium enhancement at $[\text{Fe}/\text{H}] = -1.75^{*,**}$

W. Chantereau¹, C. Charbonnel^{1,2}, and T. Decressin³

¹ Department of Astronomy, University of Geneva, Chemin des Maillettes 51, 1290 Versoix, Switzerland
e-mail: william.chantereau@unige.ch

² IRAP, UMR 5277 CNRS and Université de Toulouse, 14 Av. E. Belin, 31400 Toulouse, France

³ INAF-Osservatorio Astronomico di Roma, via di Frascati 33, 00040 Monteporzio, Italy

Received 20 February 2015 / Accepted 23 March 2015

ABSTRACT

Context. Our understanding of the formation and early evolution of globular clusters (GCs) has been totally overthrown with the discovery of the peculiar chemical properties of their long-lived host stars.

Aims. As a consequence, the interpretation of the observed color-magnitude diagrams and of the properties of the GC stellar populations requires the use of stellar models computed with relevant chemical compositions.

Methods. We present a grid of 224 stellar evolution models for low-mass stars with initial masses between 0.3 and 1.0 M_{\odot} and initial helium mass fraction between 0.248 and 0.8 computed for $[\text{Fe}/\text{H}] = -1.75$ with the stellar evolution code STAREVOL. This grid is made available to the community.

Results. We explore the implications of the assumed initial chemical distribution for the main properties of the stellar models: evolution paths in the Hertzsprung-Russel diagram (HRD), duration and characteristics of the main evolutionary phases, and the chemical nature of the white dwarf remnants. We also provide the ranges in initial stellar mass and helium content of the stars that populate the different regions of the HRD at the ages of 10 and 13.4 Gyr, which are typical for Galactic GCs.

Key words. stars: evolution – stars: abundances – stars: low-mass – globular clusters: general

1. Multiple stellar populations in globular clusters: definitions and possible origins

Globular clusters (GCs) are described in classical textbooks as old, massive, tightly bound systems hosting single stellar populations, i.e., coeval stars sharing the same initial chemical composition. These objects are extensively used as ideal benchmarks for stellar evolution theory, and their estimated absolute and relative ages provide markers for the formation and evolution of their host galaxies and their substructures (e.g., Kruijssen 2014).

This idealistic picture has been shaken with the discovery of multiple stellar populations in individual Galactic GCs thanks to high-resolution observations either with the *Hubble* Space Telescope or from the ground. Deep photometric studies have revealed the presence of multiple sequences or spreads at the turn-off and/or along the subgiant branch in the color-magnitude diagrams (CMDs) of several GCs (e.g., Bedin et al. 2004; D'Antona et al. 2005; Piotto et al. 2007; Villanova et al. 2007; Milone et al. 2008, 2010, 2013; Piotto 2008, 2009; Dalessandro et al. 2011; King et al. 2012). In addition, spectroscopic analysis is now commonly used to differentiate between so-called first- and second-generation GC stars (hereafter 1G and 2G) based on their

positions along the well-documented O-Na anti-correlation (e.g., Prantzos & Charbonnel 2006; Carretta et al. 2009b; Carretta 2013). This remarkable chemical pattern, which has been observed so far only among GC stars (see, e.g., Bragaglia et al. 2014; MacLean et al. 2015, and references therein)¹, is advocated to be the main feature that distinguishes GCs from other stellar systems (e.g., Carretta et al. 2010).

Together with the C-N and Mg-Al anti-correlations, it is interpreted as the signature of hydrogen-burning at high temperature in massive, fast-evolving 1G GC stars (hereafter referred to as polluters) whose ejecta (depleted in carbon, oxygen, and magnesium, and enriched in nitrogen, sodium, aluminum, and helium) mixed to various degrees with original intra-cluster material and gave birth to 2G stars (e.g., Prantzos et al. 2007).

Different scenarios of secondary star formation invoke different types of 1G polluters, namely fast rotating massive stars (FRMS) with initial masses above 25 M_{\odot} (Maeder & Meynet 2006; Prantzos & Charbonnel 2006; Decressin et al. 2007a,b; Krause et al. 2013), massive asymptotic giant branch (AGB) stars with initial masses between ~ 6 and 11 M_{\odot} (Ventura et al. 2001, 2013; D'Ercole et al. 2010, 2011, 2012; Ventura & D'Antona 2011), and supermassive stars with initial masses around 10⁴ M_{\odot} (Denissenkov & Hartwick 2014). In some cases the possible contribution of massive binary stars

* Appendix A is available in electronic form at <http://www.aanda.org>

** Table 3 is only available at the CDS via anonymous ftp to cdsarc.u-strasbg.fr (130.79.128.5) or via <http://cdsarc.u-strasbg.fr/viz-bin/qcat?J/A+A/578/A117>

¹ This feature has also recently been discovered among a small fraction of halo field stars (up to 2.5% of the star sample); see, e.g., Carretta et al. (2010), Martell & Grebel (2010), Ramírez et al. (2012).

(de Mink et al. 2009; Izzard et al. 2013), of FRMS paired with AGB stars (Sills & Glebbeek 2010), and of FRMS paired with high-mass interactive binaries (Bastian et al. 2013b; Cassisi & Salaris 2014) are also considered.

Several studies have suggested that the concept of stellar generations may not be appropriate to describe the long-lived stellar populations we are observing today in GCs, as this implies discontinuous star-forming events or long-term star formation. In particular the need for multiple star-forming episodes occurring 30–100 Myr after the formation of the 1G, as required by the AGB scenario, is in conflict with the star formation history derived for young massive clusters in the Milky Way and in Local Group galaxies (e.g., Bastian et al. 2013a; Cabrera-Ziri et al. 2014). An additional difficulty of this delayed star formation scenario lies in the need to re-accrete Galactic gas with exactly the same chemical composition as that of the original proto-GC material (e.g., D’Ercole et al. 2011, 2012) after several tens of Myrs and in any case after the expulsion of the original gas and of the SNe ejecta by SNe explosions or dark-remnant activation (Krause et al. 2013). The probability that this has happened for all individual GCs during their Galactic journey is actually very small.

At the opposite end in the FRMS scenario, the formation of the sodium-rich, oxygen-poor low-mass stars (so-called 2G stars) is predicted to be completed before fast gas expulsion within ~ 3.5 –8 Myr after the formation of the polluters (Krause et al. 2013). This timescale is compatible with the fact that very massive star clusters with ages of only a few Myrs in nearby galaxies appear to be devoid of gas (Bastian & Strader 2014; Bastian et al. 2014). It is also shorter than the pre-main sequence evolution of the long-lived low-mass stars we observe today in GCs²; low-mass stars formed out of original gas and those formed out of polluted material in the immediate vicinity of the FRMS should therefore have arrived on the zero age main sequence with very small time delay compared to the typical age of a GC of ~ 13.4 Gyr. It was also proposed that the ejecta of FRMS and/or high-mass interacting binaries were actually accreted by low-mass pre-main sequence stars of the same generation (Bastian et al. 2013b; see also Scenario II of Prantzos & Charbonnel 2006)³, in which case the concept of distinct stellar generations is also misleading. Last but not least, in the FRMS polluter model a large percentage of (if not all) the stars exhibiting low sodium abundance (and that are therefore counted as 1G members; see Prantzos & Charbonnel 2006; Carretta et al. 2009b) could have formed from pristine material mixed with the H-burning ashes of the fast-evolving 1G polluters (Charbonnel et al. 2014); in this case GCs would be formally devoid of 1G low-mass stars, their hosts being actually secondary star formation products with chemical properties spanning the whole range of the observed O-Na anti-correlations.

Consequently, to avoid conceptual as well as semantic ambiguities, we adopt the denominations “first population” (hereafter 1P) for the stars that were born with the original composition of the proto-GC, and “second population” (2P) for the stars that are born from a mixture between original material and the ejecta of short-lived 1P polluter stars.

² The pre-main sequence lifetimes of our $0.8 M_{\odot}$ models computed at the metallicity of NGC 6752 with initial helium mass fractions of 0.248, 0.4, and 0.8 are $\sim 1.045 \times 10^8$, 4.32×10^7 , and 2.87×10^6 yrs, respectively (see Sect. 4).

³ A possible difficulty is that in this case a very short accretion phase (~ 1 –2 Myr) is necessary to account for helium enrichment and for the observed Li-Na anti-correlation (D’Antona et al. 2014; Cassisi & Salaris 2014; Salaris & Cassisi 2014).

2. The importance of quantifying helium variations among GC stars

2.1. Dependence of the initial helium spread on the polluter scenario

Despite the many differences between the scenarios that have been developed to explain the abundance properties of GCs, it is widely accepted that the Na-enriched (2P) GC stars have started their life with a higher helium content than their 1P counterparts (this is actually obvious as helium is the main product of hydrogen burning). This has been confirmed by direct spectroscopic measurements of non-local thermodynamic equilibrium He abundances for a subset of blue horizontal branch stars in one GC (NGC 2808; Marino et al. 2014). However the initial helium distribution among 2P stars is not well known yet, as predictions for the extent of helium enrichment along the sodium distribution in 2P stars strongly depend on the nature of the invoked 1P polluters.

In the case of the AGB scenario, the quantity of helium released by the polluters is set during the second dredge-up episode on the early AGB; it amounts to a maximum of ~ 0.36 – 0.38 in mass fraction, independently of the initial mass of the AGB progenitor (e.g., Doherty et al. 2014). On the other hand, the sodium content of the ejecta of the polluter results from the competition between hot-bottom-burning and third dredge-up episodes that may occur during the later thermal-pulse AGB (TP-AGB) phase; therefore, it strongly depends on the initial mass of the polluter (Forestini & Charbonnel 1997; Siess 2007; D’Ercole et al. 2010; Ventura et al. 2013). Consequently, 2P stars spanning a large range of Na abundances are all expected to be born with very similar helium contents (maximum of 0.36 – 0.38 in mass fraction if no dilution with the ISM matter is taken into account compared with ~ 0.248 for 1P stars; see Sect. 3.2.1).

In contrast, in the FRMS scenario the enrichment in sodium and helium of the polluters’ ejecta results from central hydrogen-burning on the main sequence. Therefore this model predicts broad and correlated spreads in both sodium and helium among 2P stars at birth. In the case of NGC 6752, for example, 2P stars are expected to be born with initial helium mass fractions ranging between 0.248 (as for the 1P) and 0.8 (Decressin et al. 2007b). Such a large helium dispersion correlated with the sodium spread provides a straightforward explanation to the lack of sodium-rich 2P AGB stars in this GC (Charbonnel et al. 2013; observations by Campbell et al. 2013) due to the impact of the initial helium content on the stellar lifetime and evolution path in the Hertzsprung-Russel diagram. Simultaneously, the FRMS scenario predicts that today (i.e., at a typical GC age of 13.4 Gyr), 95% of the low-mass stars lying two magnitudes below the turn-off should be born with a helium mass fraction Y_{ini} between 0.248 and 0.4, and only 5% with Y_{ini} higher than 0.4 (Charbonnel et al. 2013). Additionally (see Sect. 5), no star born with Y_{ini} higher than 0.4 is expected to lie today on the horizontal branch, in agreement with current interpretations of GC horizontal branch (HB) morphologies in connection with the so-called second parameter problem (e.g., D’Antona et al. 2002; D’Antona & Caloi 2004; Caloi & D’Antona 2007; Gratton et al. 2010; Dotter et al. 2010).

2.2. Objectives of the present series of papers

The aim of this series of papers is to investigate the implications of the initial helium spread predicted by the FRMS scenario in different parts of the GC CMD, and at various ages along

GC evolution. Predictions will be compared to those of the AGB scenario and to available relevant observations, and future observational tests will be suggested.

Here (Paper I) we present a grid of low-mass, low-metallicity stellar models that will be extensively used for different purposes in the series. These models are computed with a $[\text{Fe}/\text{H}]$ value of -1.75 close to that of the well-studied GC NGC 6752 and for a wide range of initial helium abundance, taking into account the corresponding variations expected within the FRMS model for the elements involved in the CNO cycle and the NeNa and MgAl chains (see Sect. 3 for a detailed description of the initial chemical compositions and the input physics of the stellar models). We discuss the impact of the initial chemical composition on the characteristics, lifetimes, evolution behavior, and fate of GC low-mass stars; we first focus on the case of a $0.8 M_{\odot}$ star (Sect. 4), and then present the dependence on the initial stellar mass (Sect. 5). Although the influence of initial helium abundance on the stellar properties has already been extensively described in the literature (e.g., Iben & Faulkner 1968; Iben & Rood 1969; Demarque et al. 1971; Sweigart 1978; D’Antona et al. 2005; Caloi & D’Antona 2007; Salaris & Cassisi 2005; Maeder 2009; Pietrinferni et al. 2009; Sbordone et al. 2011; Valcarce et al. 2012; Cassisi et al. 2013; Kippenhahn et al. 2013), to our knowledge this is the first investigation of the impact of helium content higher than ~ 0.42 on the whole evolution (from the pre-main sequence to the end of the AGB phase) at low $[\text{Fe}/\text{H}]$, and for such a broad mass range⁴.

3. Grid of 1P and 2P low-mass stellar models at $[\text{Fe}/\text{H}] = -1.75$

3.1. Generalities

We present a grid of standard stellar models (i.e., with no atomic diffusion or rotation, and no overshooting) with initial masses between 0.3 and $1.0 M_{\odot}$ (mass steps of $0.05 M_{\odot}$) for $[\text{Fe}/\text{H}]$ close to that of NGC 6752, and with Y_{ini} ranging between 0.248 and 0.8 and the abundances of the elements included in the CNO, NeNa, and MgAl chains that change accordingly (see Sect. 3.2 for details on the initial chemical mixture assumed in the computations). The models are computed from the pre-main sequence up to the tip of the TP-AGB or the planetary nebula phase with the evolution code STAREVOL (e.g., Palacios et al. 2006). Mass loss is treated assuming the Reimers (1975) formula (η parameter of 0.5) on the red giant branch (RGB) and during central helium-burning, and the Vassiliadis & Wood (1993) prescription on the AGB. The basic input physics (nuclear reaction rates, equation of state, opacities, mass-loss prescriptions) is the same as in Lagarde et al. (2012), except for the mixing length parameter (1.75 here, as assumed in the FRMS models of Decressin et al. 2007b, instead of 1.6).

3.2. Initial chemical composition

3.2.1. 1P models

The initial composition of 1P stellar models must reflect that of the original intra-cluster gas. We assume an initial helium mass fraction Y_{ini} of 0.248 (i.e., slightly higher than the primordial helium abundance 0.2463 ± 0.0003 predicted by standard BBN by Coc et al. 2013 using the new value of Ω_b determined by

⁴ D’Antona et al. (2010) have investigated the effect of a Y up to 0.8 , but only on the horizontal branch morphology.

Planck Collaboration XVI 2014). In order to be consistent with Decressin et al. (2007b) we adopt a scaled-solar abundance composition (Grevesse & Noels 1993), a heavy element mass fraction Z of 5×10^{-4} , and an alpha-enhancement of $[\alpha/\text{Fe}] = +0.3$. This corresponds to $[\text{Fe}/\text{H}] = -1.75$, close to the value of -1.56 derived for NGC 6752 (e.g., Carretta et al. 2007, 2009a; Villanova et al. 2009).

3.2.2. 2P models

Following Prantzos & Charbonnel (2006) and Decressin et al. (2007a,b), we assume that the initial chemical composition of 2P stars consists of a time-dependent mixture between a) the intra-cluster material of the original composition and b) the material processed to various degrees through central H-burning and progressively ejected by the FRMS during their mechanically-driven slow wind phase (i.e., along the main sequence and the $\Omega\Gamma$ -limit phase). As FRMS release the first material of original GC composition at the very beginning of their evolution, and later material richer in H-burning ashes, one expects 2P stars with Na and He contents similar to that of 1P stars to form first, and then 2P stars with various degrees of Na and He enrichment (see, e.g., Charbonnel et al. 2014).

To account for this general behavior, we assume that the initial mass fraction of a given isotope i in 2P stars varies from star to star according to

$$X_i^{2P} = X_i^{\text{wind}} (1 - a_t) + X_i^{\text{ICM}} a_t, \quad (1)$$

with the various terms described below.

- The original intra-cluster medium value X_i^{ICM} is equal to X_i^{1P} assumed for 1P stars (Sect. 3.2.1).
- For the mass fraction of the isotope i in the massive star ejecta, X_i^{wind} , we use the time-dependent predictions along the main sequence and the $\Omega\Gamma$ -limit phase of the $60 M_{\odot}$ 60rC model FRMS model of Decressin et al. (2007b) computed with the Set C of nuclear reactions (see their Table 2, and the discussion in Sect. 3.2.3). In order to cover the highest helium enrichment, we also take into account the part of the ejecta of their $120 M_{\odot}$ 120rC FRMS model that correspond to a helium mass fraction higher than 0.88 (i.e., the maximum value for the $60 M_{\odot}$ star; see Fig. 1).
- The dilution factor a_t varies during the lifetime of individual 1P polluters between 0.99 (ejecta strongly diluted with the surrounding intra-cluster gas) and a minimum value a_{min} of 0.2 that is constrained by the Na-Li anti-correlation observed in NGC 6752 turn-off stars (observations by Pasquini et al. 2005; see, e.g., Decressin et al. 2007b).

The resulting range for the initial abundances of C, N, O, Na, Mg, and Al of our 2P stellar models is shown in Fig. 1 as a function of the initial mass fraction of helium. For each stellar mass between 0.3 and $1.0 M_{\odot}$ (mass steps of $\sim 0.05 M_{\odot}$, i.e., 14 initial masses), we compute 16 models with initial helium abundance varying between 0.248 and 0.8 (steps ≤ 0.05 , actual Y_{ini} values indicated by the black points in Fig. 1). Therefore, our grid consists of 224 stellar models in total.

3.2.3. Comparison with spectroscopic abundances in NGC 6752

Within the FRMS scenario, 2P low-mass stars are expected to form in the immediate vicinity of the massive star polluters, which might actually all evolve in different environments

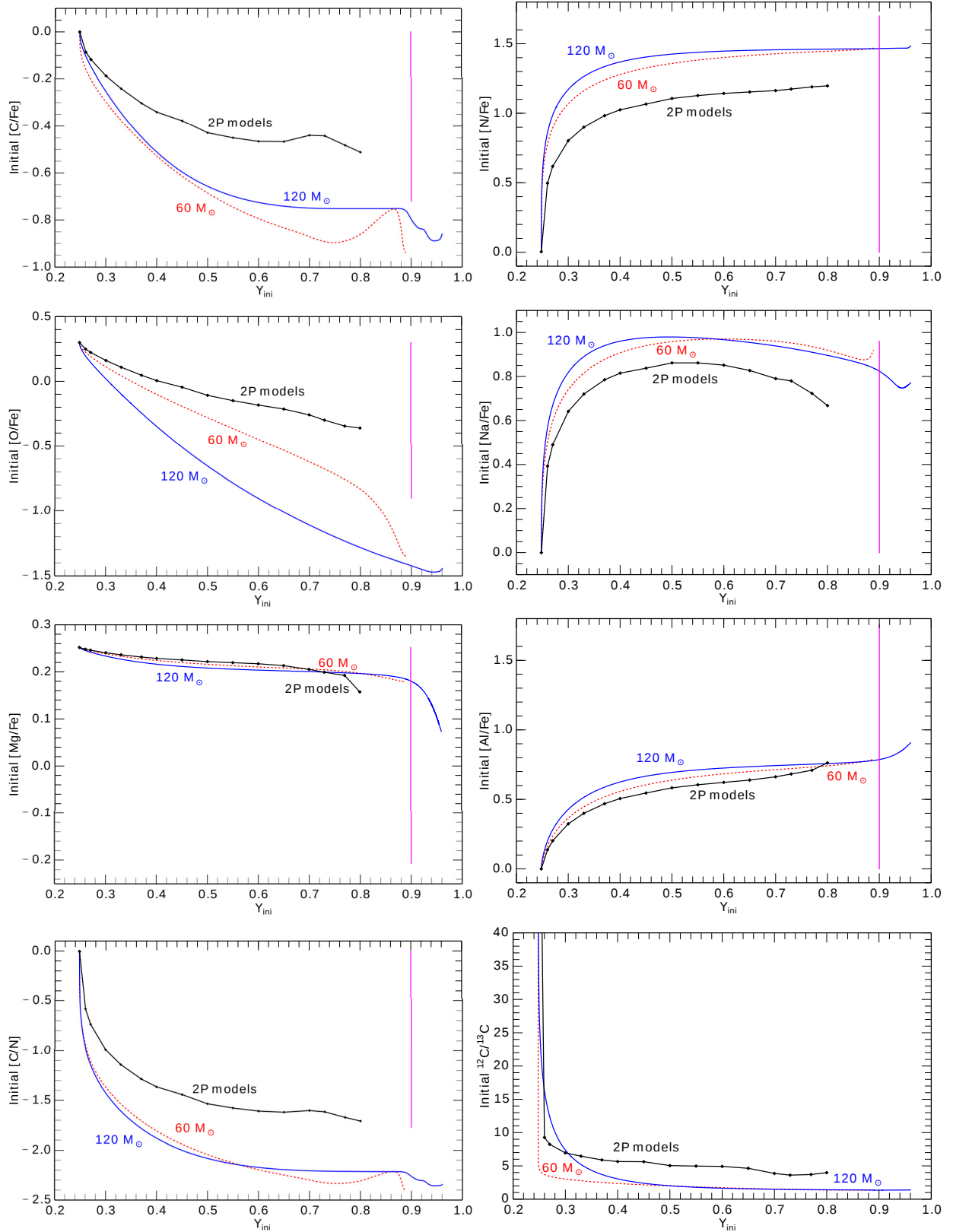


Fig. 1. Theoretical distribution for the initial carbon, nitrogen, oxygen, sodium, magnesium, and aluminum abundances ($[X/Fe] = \log(X/Fe)_* - \log(X/Fe)_\odot$ for $[C/N]$ and for $^{12}C/^{13}C$ (initial value of 90) as a function of the initial helium mass fraction adopted for our 2P stars models (black line; dots indicate the 16 values adopted for the model computations of each stellar mass between 0.3 and 1 M_\odot). This accounts for dilution between original 1P material and the ejecta of the 60 and 120 M_\odot FRMS models (red and blue lines, respectively; Decressin et al. 2007b) as described in Eq. (1) (see text). The magenta arrows represent the variations observed in NGC 6752 for $[C/Fe]$ and $[N/Fe]$ (Carretta et al. 2005), $[O/Fe]$ and $[Na/Fe]$ (Carretta et al. 2007), and $[Mg/Fe]$ and $[Al/Fe]$ (Carretta et al. 2012).

(e.g., in terms of pristine gas available), depending on their orbit (Krause et al. 2013). Individual FRMS polluters of similar initial masses are thus expected to give birth to 2P of slightly different compositions as a result of the peculiar mixing between individual winds and pristine material (in other words, a_t and a_{\min} might vary for individual polluters).

Therefore, the abundance variations covered by our grid of 2P stellar models represent the mean trends for all chemical elements, but do not cover the most extreme abundance variations that could be reached in the case of 2P stars formed out of raw FRMS ejecta, for example. This can be seen in Fig. 1, where the initial chemical composition for our 2P models is compared with the maximum abundance variations that have been found among main sequence and red giant stars in NGC 6752 (respectively 0.7, 1.7, 1.2, 1.0, 0.46, and 1.8 dex for C, N, O, Na, Mg, and Al; Carretta et al. 2005, 2007, 2012). As discussed in Decressin et al. (2007b), the observed variations in Mg and Al require an increase in the ^{24}Mg burning rate with respect to the experimental values (their $60 M_{\odot}$ 60rD model), which is not accounted for in the $60 M_{\odot}$ 60rC model used in Sect. 3.2.2. However, this will not affect any of our findings since the Mg and Al content has no impact on the stellar evolution tracks or on the stellar lifetimes.

4. Impact of extreme helium enrichment on stellar properties all along the evolution: the $0.8 M_{\odot}$ case

As mentioned above, several studies of the influence of the initial helium content on stellar properties can be found in the literature, but only for relatively modest helium enrichment or for specific evolutionary phases. Here we recall the main trends and explore in detail the impact of very high initial helium content (i.e., mass fraction ≥ 0.4) all along the evolution. We first describe here the $0.8 M_{\odot}$ case, which is the typical GC turn-off mass found in the literature⁵, and later discuss the various evolution paths depending on the initial stellar mass (Sect. 5). The limits of the various evolutionary phases are chosen as follows:

- the ZAMS is defined either by a central mass fraction of hydrogen that has decreased by 0.6% compared to its surface value, or by a central temperature that has reached 3×10^7 K;
- the turn-off is reached when the central mass fraction of hydrogen is lower than 10^{-7} ;
- the end of the subgiant branch (SGB, base of the RGB) is the moment when the mass coordinate at the top of the H-burning shell (i.e., when $\leq 10 \text{ erg g}^{-1} \text{ s}^{-1}$) reaches a local minimum.
- the zero age horizontal branch (ZAHB) corresponds to the point where the helium mass fraction at the center of the star is 0.8.

Figure 2 shows the evolution tracks of all the $0.8 M_{\odot}$ models that we computed with the 16 different initial compositions described in Sect. 3.2.2; for clarity we also show the tracks of three selected cases corresponding to $Y_{\text{ini}} = 0.248, 0.4,$ and 0.8 .

4.1. Main sequence

When the initial helium content is higher, the opacity due to Thomson scattering is reduced in the stellar interior, and the nuclear burning luminosity increases during the main sequence

⁵ Our $0.8 M_{\odot}$ 1P model with $Y_{\text{ini}} = 0.248, Z = 5 \times 10^{-4}$ leaves the main sequence at an age of 13 Gyr.

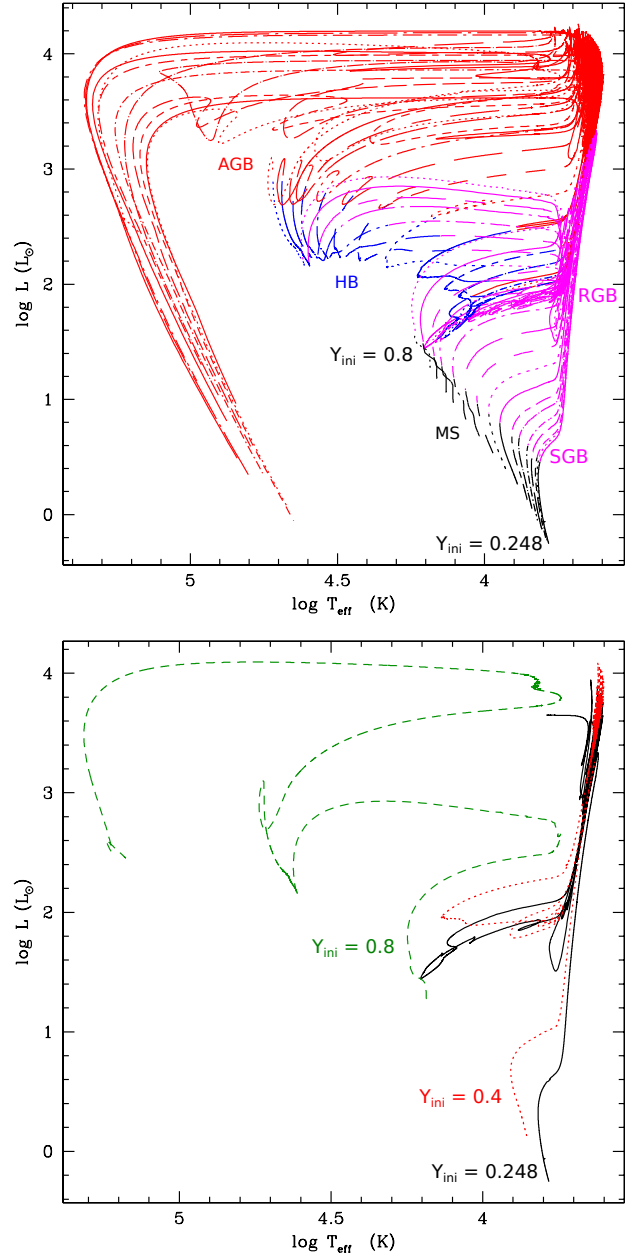


Fig. 2. *Top:* evolution in the HRD of the $0.8 M_{\odot}$ models for 16 different Y_{ini} between 0.248 and 0.8 ($Z = 5 \times 10^{-4}$). Colors depict the evolutionary phases (main sequence in black, subgiant and red giant branch in magenta, central helium burning in blue, post central helium burning in red; the pre-main sequence is not shown for clarity). *Bottom:* $0.8 M_{\odot}$ models computed with $Y_{\text{ini}} = 0.248, 0.4,$ and 0.8 (black, red, and green, respectively).

because of the greater mean molecular weight⁶. Consequently, the evolution tracks are shifted towards higher luminosities and effective temperatures, and the main sequence lifetime is significantly shortened as shown in Fig. 3: while the $0.8 M_{\odot}$ model with $Y_{\text{ini}} = 0.248$ spends 12.9 Gyr on the main sequence (90% of its total lifetime), those with $Y_{\text{ini}} = 0.4$ and 0.8 have main sequence lifetimes of 4.62 Gyr and 158 Myr, respectively, which corresponds to 86% and 60% of their total evolution.

During the main sequence, the internal temperature profiles steepen and higher central temperatures are reached for higher

⁶ The homology relations give $L \propto \mu^{7.3}$ and $L \propto \mu^{7.8}$ when the pp chain or the CNO cycle dominates; see, e.g., Mowlavi et al. (1998).

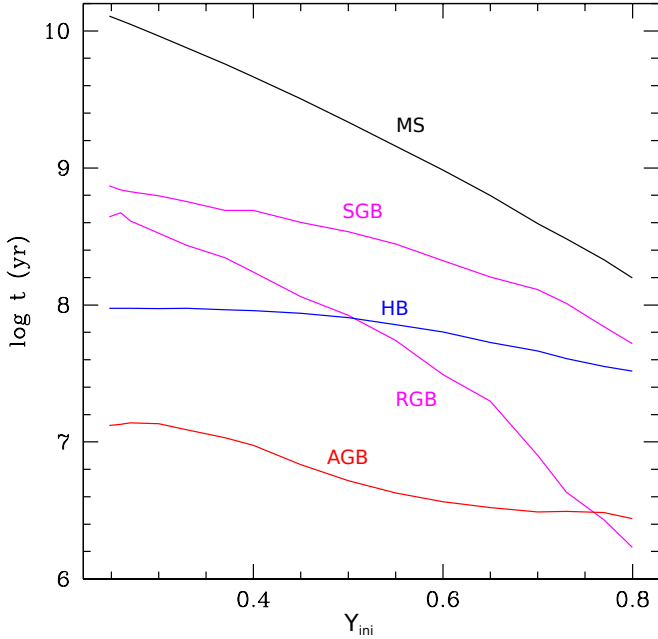


Fig. 3. Duration of each evolutionary phase of the $0.8 M_{\odot}$ models as a function of their initial helium mass fraction (main sequence, subgiant branch, red giant branch, horizontal branch, and asymptotic giant branch are shown in black, magenta, blue, and red, respectively).

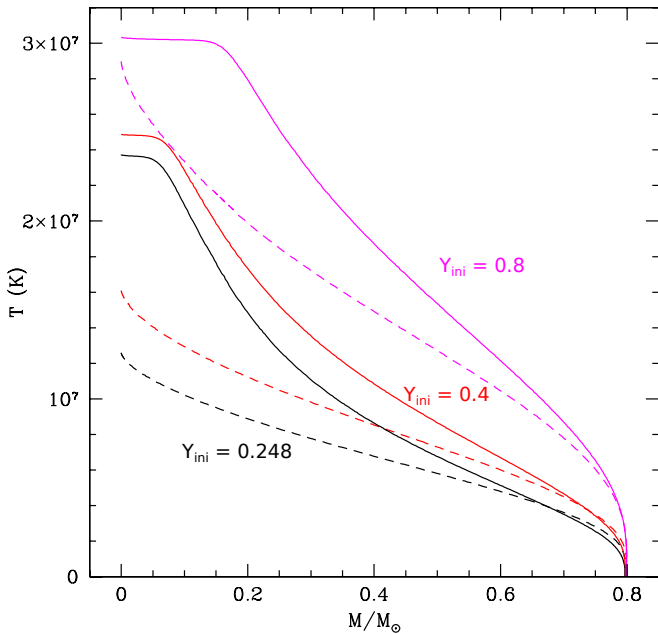


Fig. 4. Temperature profiles at the zero age main sequence (dashed line) and at the turn-off (solid) inside the $0.8 M_{\odot}$ models computed with the three different initial helium mass fractions.

initial helium content (Figs. 4 and 5). This modifies the nuclear burning mode and the internal stellar configuration, as can be seen in the Kippenhahn diagrams presented in Fig. 6 for the three $0.8 M_{\odot}$ models computed with $Y_{\text{ini}} = 0.248, 0.4,$ and 0.8 . While the first two burn central hydrogen mainly through the pp-chain and have a radiative core on the main sequence, the super He-rich model burns hydrogen only through the CNO cycle in a convective core (the transition occurs at $Y_{\text{ini}} = 0.5/0.55$). In addition, when Y_{ini} is higher, the effects of central hydrogen burning are less pronounced because the initial abundances of

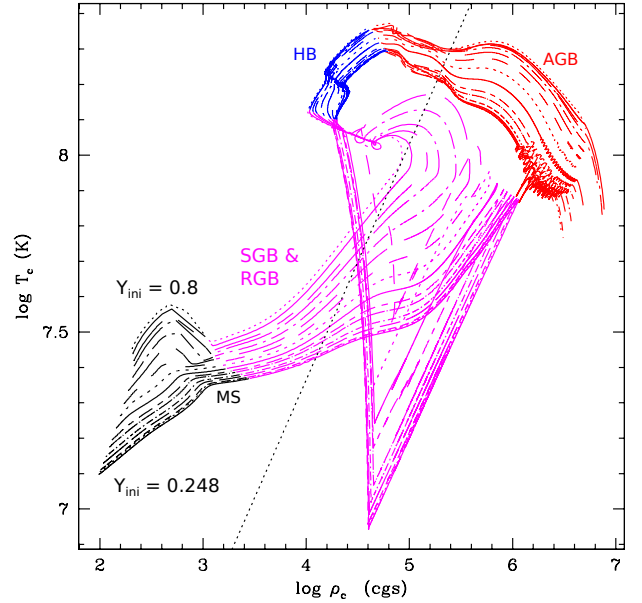


Fig. 5. Central temperature as a function of the central density along the evolution of the $0.8 M_{\odot}$ models computed with various initial helium mass fractions from 0.248 to 0.8 (colors correspond to evolutionary phases as in Fig. 2); the bend at the end of the RGB is characteristic of the helium flash. The straight dotted line corresponds to the limit where the pressure given by the non-relativistic perfect gas law is equal to the pressure given by the completely degenerate non-relativistic gas, and where the mean molecular weight is of the core of a RGB star, i.e., $\log(T_c) = 4.7 + 2/3 \log(\rho_c)$.

all the isotopes involved in the CNO-cycle and the NeNa and MgAl chains are closer to their equilibrium values. We recall that the initial metal mixture at varying Y_{ini} is obtained from the dilution of matter coming from the H-burning regions of massive stars with pristine gas. Consequently, the internal chemical profiles of the various models strongly differ at the end of the main sequence (Fig. 7), which will have an impact during the advanced evolutionary phases.

4.2. Subgiant and red giant branches

The models with higher initial helium content cross the Hertzsprung gap (subgiant branch) at higher luminosity. Although the first dredge-up occurs in all the $0.8 M_{\odot}$ models of our grid, its effects on the surface abundances are smoothed out for higher Y_{ini} owing to shallower convective envelopes (see in Fig. 7 the vertical arrows that indicate the maximum depth reached by the convective envelope during the first dredge-up; see also Figs. 6 and 8) and to initial chemical abundances closer to or already at equilibrium. This is quantified in Table 1, which summarizes the variations of the surface abundances during this phase for the three selected $0.8 M_{\odot}$ models.

The characteristics of the RGB bump are consequently affected. While the $0.8 M_{\odot}$ models with $Y_{\text{ini}} \lesssim 0.4$ undergo a drop in their total luminosity when the hydrogen-burning shell crosses the chemical discontinuity left inside the star by the convective envelope during the first dredge-up (Fig. 14), the super He-rich stars do not and have a constant increase of luminosity along the RGB evolution (see the characteristics of the bump in Table 2 and Fig. 9).

In the same way as for the other evolutionary phases, the lifetimes on the subgiant and the RGBs shorten when Y_{ini} increases (Fig. 3). This results from lower degeneracy and higher central

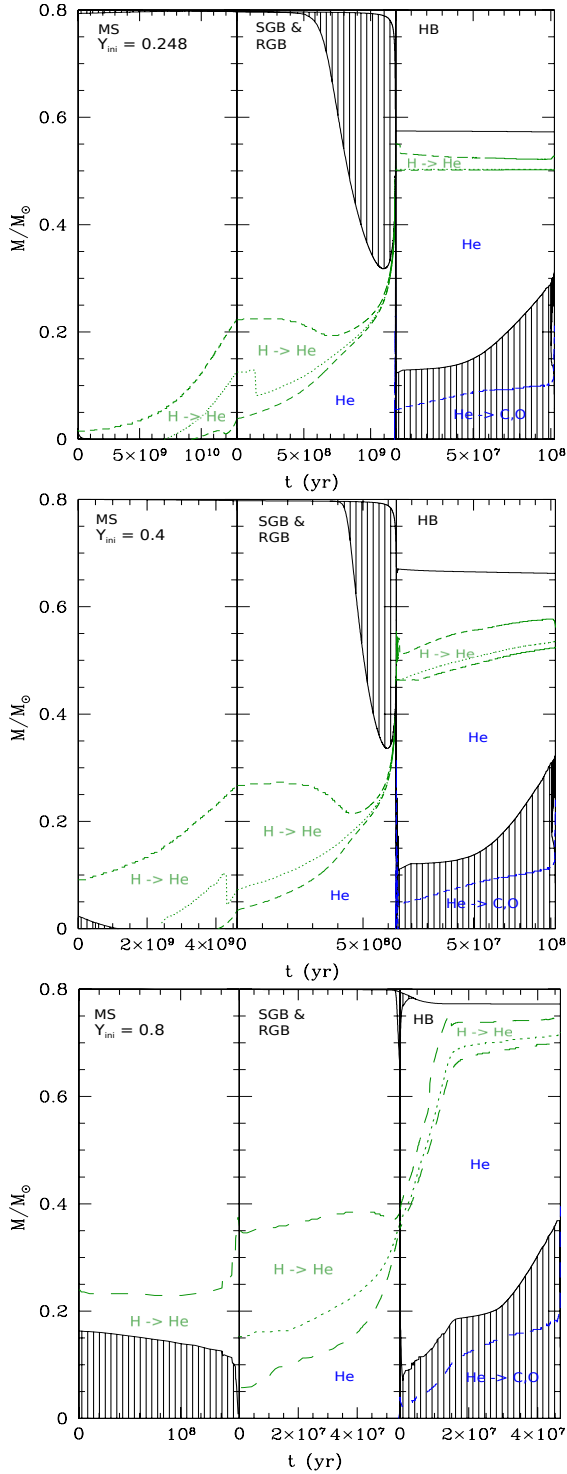


Fig. 6. Internal properties (Kippenhahn diagram) of the $0.8 M_{\odot}$ models with $Y_{\text{ini}} = 0.248, 0.4,$ and 0.8 (top, middle, bottom) from the zero age main sequence to the end of central-helium burning. Green dashed lines delimit hydrogen burning regions ($\geq 10 \text{ erg g}^{-1} \text{ s}^{-1}$); blue dashed lines delimit the helium burning regions ($\geq 10^3 \text{ erg g}^{-1} \text{ s}^{-1}$); dotted green and blue lines show the maximum energy production of H- and He-burning; hatched areas represent the convective zones. Timescales give the duration of each evolutionary phase.

temperature of the helium core (Fig. 5), which lead to smooth central helium ignition occurring at lower stellar luminosity for the super He-rich $0.8 M_{\odot}$ models, while the models with Y_{ini} below $\sim 0.5/0.55$ undergo the so-called helium flash at the RGB tip

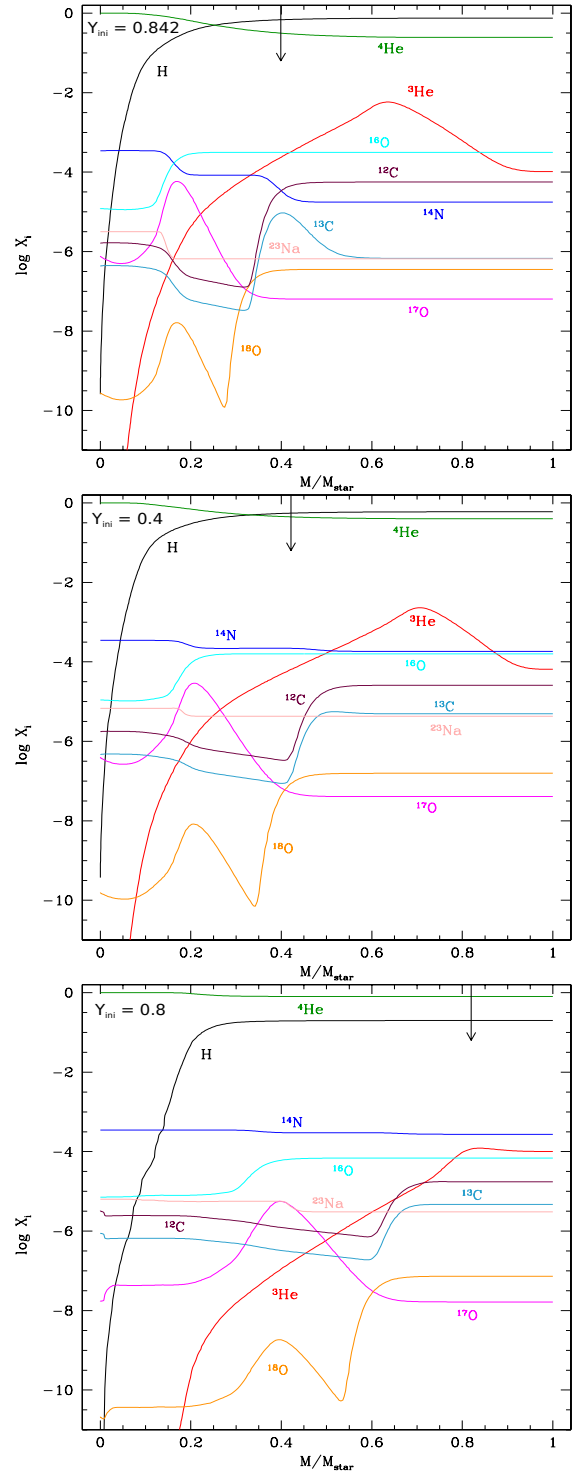


Fig. 7. Abundance profiles of the main chemical elements as a function of depth in mass at the end of the main sequence for the $0.8 M_{\odot}$ models with $Y_{\text{ini}} = 0.248, 0.4,$ and 0.8 (top, middle, bottom). The arrows indicate the maximum depth reached by the convective envelope during the first dredge-up on the red giant branch.

(see the different RGB paths in Figs. 2 and 5). Quantitatively, it takes 1.18 Gyr (8% of the total stellar lifetime) after the turn-off for the $0.8 M_{\odot}$ model with $Y_{\text{ini}} = 0.248$ to ignite helium, 663 Myr (12%) when $Y_{\text{ini}} = 0.4$, and only 53.8 Myr (20%) if $Y_{\text{ini}} = 0.8$. The amount of mass lost through the stellar wind during these phases (modeled here according to Reimers' prescription with $\eta = 0.5$) decreases because of shorter timescales and

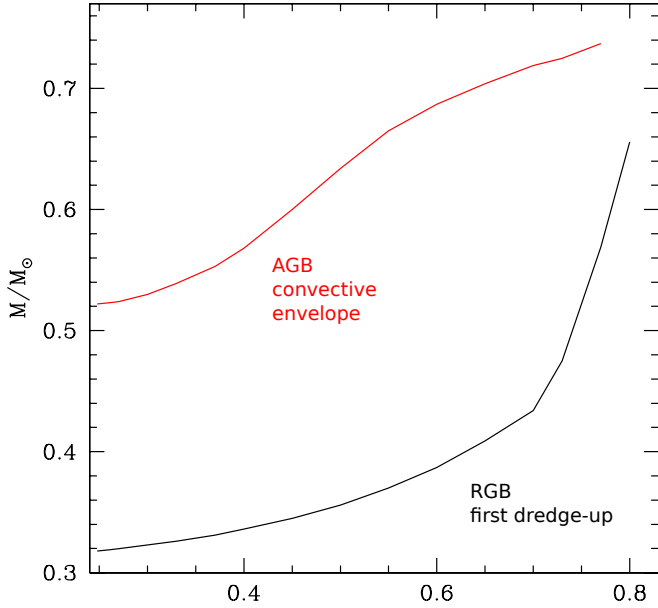


Fig. 8. Mass layer (in solar mass) within the star reached by convection at its maximum extension on the RGB and AGB as a function of the Y_{ini} for the $0.8 M_{\odot}$ models.

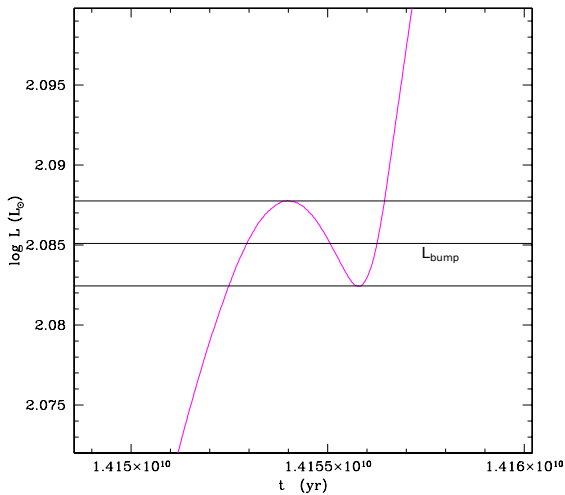


Fig. 9. Variations of luminosity during the RGB bump for the $0.8 M_{\odot}$ model with $Y_{\text{ini}} = 0.248$. The luminosity starts dropping when the H-burning shell encounters the H-abundance discontinuity left behind by the convective envelope during the first dredge-up; it increases again when this discontinuity has been crossed. In Table 2 we give the time the star spends between the lower and upper horizontal lines, as well as the luminosity of the bump indicated by the middle horizontal line.

lower luminosity ranging from 0.005 to $0.223 M_{\odot}$. Therefore, the total stellar mass at helium ignition is lower for lower initial helium content (Fig. 10).

4.3. Horizontal branch

The effective temperature and the luminosity of a star on the horizontal branch (HB) directly depend on the total stellar mass, and more importantly on the respective masses of the helium core and of the envelope above the core at central helium ignition, as well as on the opacity in the stellar envelope (Salaris & Cassisi 2005; Maeder 2009; Kippenhahn et al. 2013). For the reasons described above, these quantities strongly vary with the

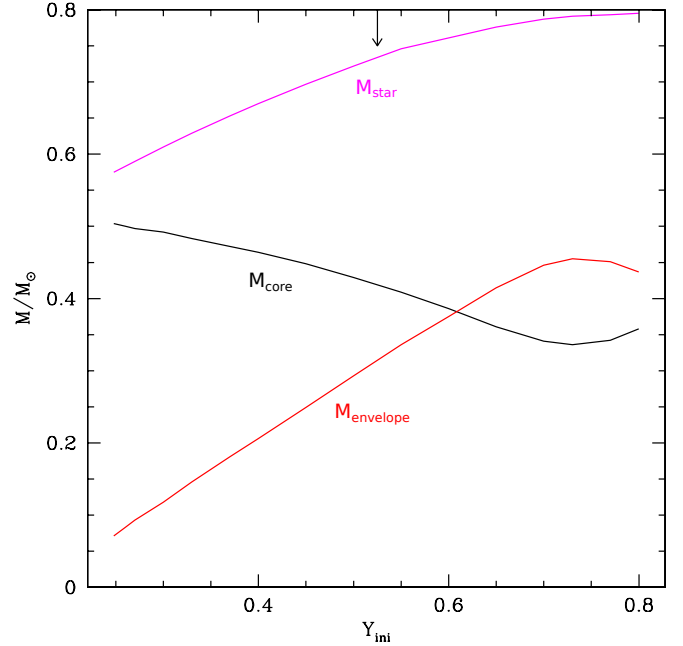


Fig. 10. Mass of the helium core (black), of the convective envelope (red), and total stellar mass (magenta) at the RGB tip (i.e., at helium ignition) for the $0.8 M_{\odot}$ models as a function of initial helium mass fraction. The arrow represents the maximum initial helium mass fraction for the He-flash to occur in the $0.8 M_{\odot}$ case.

initial helium content for a given initial stellar mass, as shown in Fig. 10 for the $0.8 M_{\odot}$ case, with consequences on the HB tracks (see Table 2 where we give the effective temperature and corresponding luminosity of the $0.8 M_{\odot}$ models on the ZAHB and at maximum T_{eff} on the HB). In the same way as for the effective temperature on the ZAHB, one can distinguish two regimes. On the one hand, the models that undergo the helium flash (Y_{ini} below $\sim 0.5/0.55$) arrive on the ZAHB with a higher total mass and a much lower $M_{\text{core}}/M_{\text{env}}$ ratio when their initial helium content was higher, therefore with a lower T_{eff} and a higher luminosity. On the other hand, for the models that do not undergo the helium flash, T_{eff} (ZAHB) increases with Y_{ini} because of a higher total mass and an increasing core mass at that phase. As a result of these two effects, the maximum effective temperature reached on the HB by the $0.8 M_{\odot}$ models presents a minimum when $Y_{\text{ini}} \sim 0.33$.

In all cases central helium burning occurs in convective conditions (right panels in Fig. 6). The resulting CO-core mass increases with increasing Y_{ini} (Fig. 12; see also Fig. 11 for the abundance profiles inside the three selected $0.8 M_{\odot}$ models at the end of central helium burning).

Finally, the lifetime on the horizontal branch is not very sensitive to the initial helium content in the domain where the stars undergo the helium flash (Y_{ini} below $\sim 0.5/0.55$), since these objects have nearly identical helium-core mass and central temperature at the arrival on the horizontal branch. However, the lifetime on the horizontal branch drops for the super helium-rich stars. For the $0.8 M_{\odot}$ models with $Y_{\text{ini}} = 0.248, 0.4,$ and 0.8 , this phase lasts respectively 94, 91, and 33 Myr (i.e., respectively 0.7%, 1.7%, and 12.5% of the total stellar lifetime).

4.4. Asymptotic giant branch

After central helium exhaustion, all the $0.8 M_{\odot}$ models with Y_{ini} below or equal to 0.6 reach the TP-AGB; $0.8 M_{\odot}$ models with

Table 1. Surface abundances of the main elements before and after the first dredge-up on the RGB for the selected $0.8 M_{\odot}$ models.

He (Mass fraction)	H		He		[C/N]		$^{12}\text{C}/^{13}\text{C}$	
	Before	After	Before	After	Before	After	Before	After
0.248	0.7514	0.7396	0.2481	0.2581	0	0	90.0	40.4
0.4	0.5994	0.5905	0.4001	0.4090	-1.30	-1.36	5.65	5.33
0.8	0.1994	0.1994	0.8001	0.8001	-1.61	-1.61	3.99	3.99

Notes. The values for hydrogen and helium are in mass fraction and those for $^{12}\text{C}/^{13}\text{C}$ are in number fraction.

Table 2. Luminosity and duration (in Myr) of the RGB bump (as defined in Fig. 9), and luminosity at the tip of the RGB.

Y_{ini}	$\log(L_{\text{bump}}/L_{\odot})$	τ_{bump}	$\log(L_{\text{tip}}/L_{\odot})$	$\log(L/L_{\odot})$ ZAHB	$\log(T_{\text{eff}})$ ZAHB (K)	M_{tot} ZAHB (M_{\odot})	M_{core} ZAHB (M_{\odot})	$\log(T_{\text{eff}})$ max-HB (K)
0.248	2.09	3.9	3.34	1.46	4.19	0.574	0.501	4.21
0.26	2.11	3.6	3.33	1.48	4.17	0.583	0.498	4.18
0.27	2.13	3.4	3.33	1.51	4.16	0.590	0.496	4.17
0.3	2.19	2.6	3.32	1.61	4.10	0.610	0.490	4.10
0.33	2.25	1.9	3.30	1.73	4.02	0.629	0.482	4.07
0.37	2.34	0.99	3.28	1.85	3.90	0.652	0.472	4.09
0.4	2.40	~	3.26	1.92	3.85	0.668	0.463	4.14
0.45	–	–	3.21	2.03	3.77	0.693	0.454	4.23
0.5	–	–	3.15	2.13	3.75	0.716	0.446	4.34
0.55	–	–	3.06	2.24	3.75	0.735	0.443	4.44
0.6	–	–	2.95	2.35	3.76	0.745	0.442	4.51
0.65	–	–	2.84	2.50	3.88	0.749	0.464	4.57
0.7	–	–	2.66	2.65	4.04	0.755	0.490	4.64
0.73	–	–	2.60	2.74	4.19	0.758	0.521	4.71
0.77	–	–	2.59	2.83	4.41	0.765	0.578	4.69
0.8	–	–	2.66	2.76	4.57	0.773	0.627	4.74

Notes. Luminosity, effective temperature, total mass, and mass of the core at the ZAHB, and finally maximum effective temperature on the HB for the $0.8 M_{\odot}$ model as a function of Y_{ini} .

higher Y_{ini} spend a short amount of time on the early-AGB before totally losing their envelope.

During the early-AGB the convective envelope deepens again in mass (except in the extreme $Y_{\text{ini}} = 0.8$ case that has expelled all its envelope at that time; see Fig. 8). No formal second dredge-up occurs, as the convective envelope does not reach the regions where helium abundance increases (see the arrows in Fig. 11), although it barely reaches the region where the CN-cycle has operated, and the surface abundances of the carbon and nitrogen isotopes slightly change once again. However, this effect is strongly attenuated when Y_{ini} increases, as in the case of the first dredge-up described above.

For the $0.8 M_{\odot}$ case, the total number of thermal pulses (TPs) first increases with the value of the initial helium content owing to higher stellar mass at the arrival on the TP-AGB. However for Y_{ini} above 0.45, this is counterbalanced by the greater ratio between the mass of the CO core and that of the very shallow envelope (Fig. 12), and the number of thermal pulses then decreases. Quantitatively, the $0.8 M_{\odot}$ with $Y_{\text{ini}} = 0.248, 0.4,$ and 0.6 undergo respectively 8, 18, and 12 thermal pulses, and the TP-AGB phase lasts 1.9, 1.35, and 0.07 Myr, respectively.

Importantly, for Y_{ini} higher than or equal to 0.65 no thermal pulse occurs and the models spend a very short time on the AGB (post-early AGB) and then evolve directly towards the white dwarf (WD) stage, which strongly reduces the probability of observing super He-rich stars on the AGB phase.

4.5. White dwarf

The mass of the degenerate CO-core at the beginning and the end of the TP-AGB phase is shown in Fig. 12 for the $0.8 M_{\odot}$

case. The mass of the CO white dwarf strongly increases with increasing initial helium content. The $Y = 0.248$ model reaches the bluest point of the evolution at 14.3 Gyr, and then starts the final cooling phase (WD cooling curve) with $M_{\text{core}} = 0.570 M_{\odot}$ whereas for the $Y = 0.4$ model this happens at 5.41 Gyr with $M_{\text{core}} = 0.659 M_{\odot}$ (Fig. 12) and at 264 Myr with $M_{\text{core}} = 0.746 M_{\odot}$ for the $Y = 0.8$ model. Evolution was not computed further except for a couple of models, since discussion of the WD cooling sequence is beyond the scope of this paper.

5. Impact of extreme helium enrichment: dependence on the initial stellar mass

Here we present the combined effects of varying both initial helium and stellar mass over the considered mass domain between 0.3 and $1.0 M_{\odot}$. We highlight the main points for specific evolutionary phases, and give the corresponding ranges in ($M; Y_{\text{ini}}$) at 10 and 13.4 Gyr that delimit the typical ages of Galactic GCs⁷. The numbers predicted for ($M; Y_{\text{ini}}$) at a given age are expected to vary with $[\text{Fe}/\text{H}]$ and are given here for the present grid computed with $[\text{Fe}/\text{H}] = -1.75$. The various ($M; Y_{\text{ini}}; \text{age}$) domains would also be slightly modified for different prescriptions of the mass-loss rates (we note that in the present computations mass loss is treated according to Reimers 1975 with $\eta = 0.5$ on the RGB and to Vassiliadis & Wood 1993 on the AGB).

⁷ The present models do not include atomic diffusion. Therefore, the ages of 10 and 13.4 Gyr should not be directly compared to those derived in the literature for specific GC from models that include the related processes. Rather, the numbers we give should be compared in terms of relative ages.

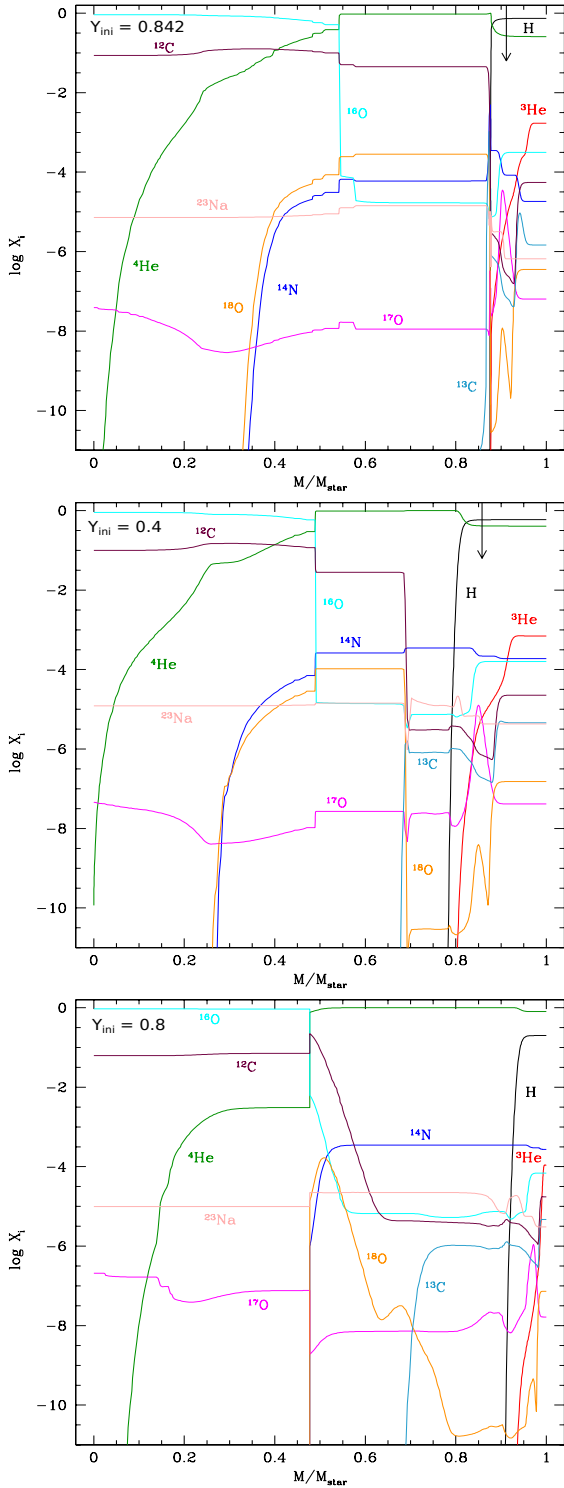


Fig. 11. Abundance profiles as a function of the depth in mass for the main chemical elements at the end of the central helium burning for the $0.8 M_{\odot}$ models with $Y_{\text{ini}} = 0.248, 0.4,$ and 0.8 (from top to bottom). The total stellar mass at this evolution point is respectively $0.573, 0.662,$ and $0.772 M_{\odot}$. The arrows indicate the maximum depth of the convective envelope during the early AGB phase.

Tracks and lifetime: similarly to the $0.8 M_{\odot}$ case, luminosity and effective temperature shifts occur in the Hertzsprung-Russel diagram (HRD) for each given initial mass when Y_{ini} increases (Fig. 13), and the duration of each evolutionary phase is reduced accordingly. In particular, the main sequence lifetime strongly

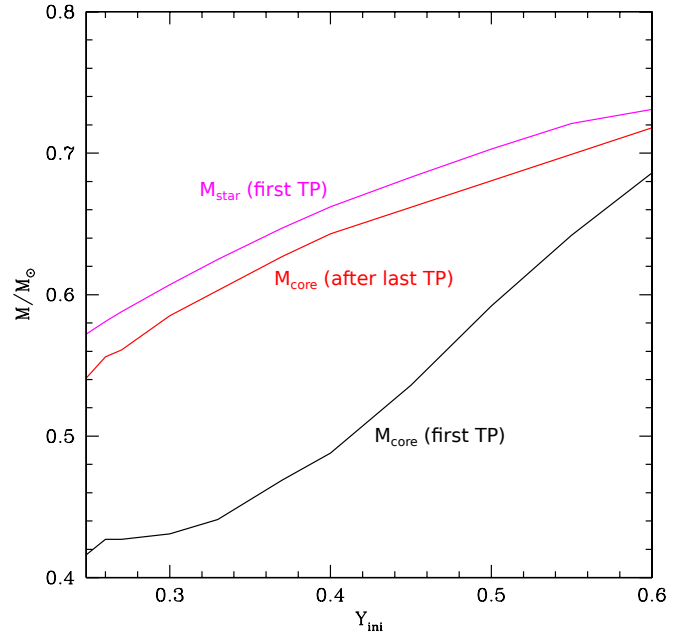


Fig. 12. CO core and total stellar mass at the first thermal pulse, and CO core mass after the last one for the $0.8 M_{\odot}$ models with Y_{ini} between 0.248 and 0.6.

depends on Y_{ini} (see the color scale in Fig. 15). For a canonical GC age of 13.4 Gyr (see the corresponding isochrone in the figure), the stars that are expected to be at the main sequence turn-off have $(M; Y_{\text{ini}})$ between $(0.794; 0.248)$ and $(0.3; 0.719)$; at 10 Gyr, these quantities are between $(0.858; 0.248)$ and $(0.3; 0.754)$.

RGB bump: the luminosity of the RGB bump increases with both initial stellar mass and initial helium content (Fig. 14). However, above a certain $(M; Y)$ threshold the stars evolve along the RGB without any luminosity drop, and the bump consequently disappears (white area in Fig. 14) as discussed in Sect. 4.2 for the $0.8 M_{\odot}$ case. The stars that are expected to be at the RGB bump have $(M; Y_{\text{ini}})$ between $(0.813; 0.248)$ and $(0.75; 0.295)$ when we consider an age of 13.4 Gyr (see isochrone), and between $(0.881; 0.248)$ and $(0.755; 0.336)$ at 10 Gyr.

RGB tip and central helium-burning ignition: the $(M; Y_{\text{ini}})$ domain where stars ignite central helium is indicated in Fig. 15 (i.e., in the area found to the right of the curve CO WD/He WD curve). For the canonical Y_{ini} value of 0.248, all the models of the considered mass range that ignite central helium-burning (i.e., $M_{\text{ini}} \geq 0.737 M_{\odot}$) do so in degenerate conditions via the so-called helium flash at the tip of the RGB. However, when the initial helium increases, low-mass stars evolve faster on the RGB; they ignite central helium burning smoothly in less degenerate conditions and at a lower luminosity. The limit in terms of $(M; Y_{\text{ini}})$ between the two regimes goes from $(0.46; 0.63)$ to $(1.0; 0.45)$ for the mass range we are interested in (Fig. 16).

Position on the horizontal branch: for a given initial stellar mass, the position on the HB strongly depends on Y_{ini} because it affects whether or not the star ignites He in degenerate conditions, and also depends on the respective masses of the helium core and of the stellar envelope when central helium-burning starts (Sect. 4.3). In particular, for the models that undergo the He flash, the higher Y_{ini} , the hotter the position on the HB. At 13.4 Gyr (and at 10 Gyr, respectively), the models that are in the central helium-burning phases have $(M; Y_{\text{ini}})$ between $(0.815; 0.248)$ and $(0.670; 0.355)$ (respectively between

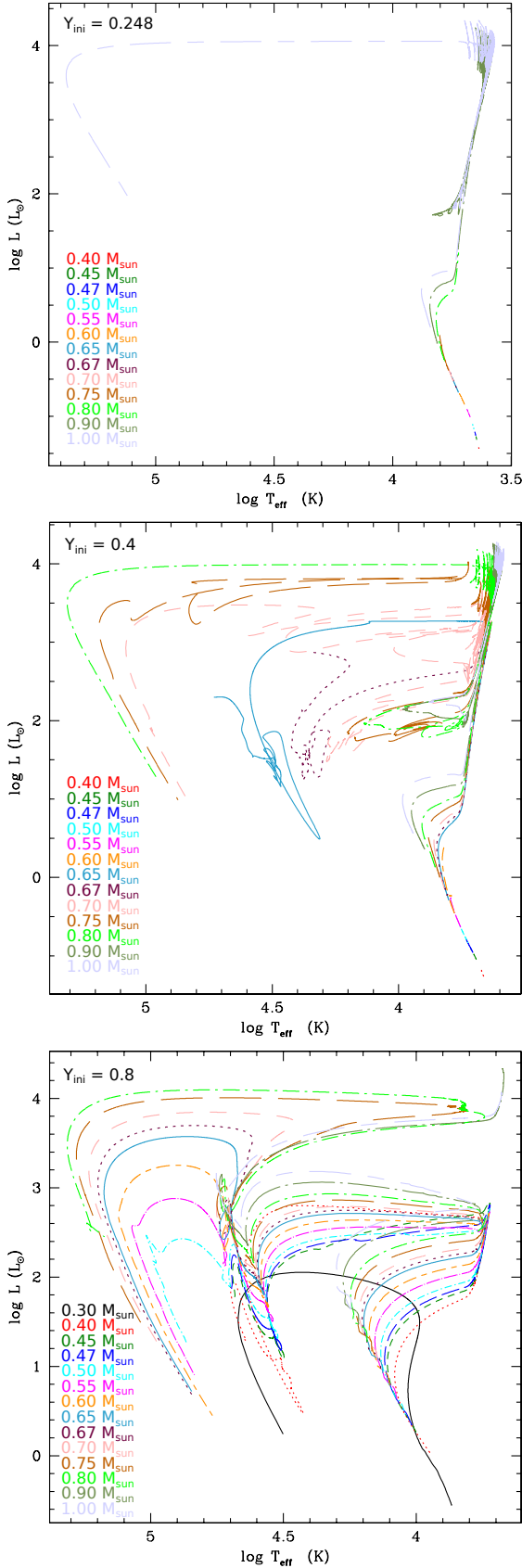


Fig. 13. Evolution in the HRD of all the models with initial stellar masses between 0.3 and $1.0 M_{\odot}$ for $Y_{\text{ini}} = 0.248$, 0.4, and 0.8 (*top*, *middle*, and *bottom*, respectively). For the very low-mass models, we stop the evolution if it exceeds 14 Gyr. At this age, the (0.3, 0.248) and (0.3, 0.4) models are still on the pre-main sequence, therefore they are not present in the HRD.

(0.884; 0.248) and (0.599; 0.458)), and the HB covers a domain in T_{eff} between 9550 and 36 310 K (respectively between 5370 and 36 310/37 150 K).

TP-AGB vs. failed-AGB: among the stars that manage to burn central helium, a significant percentage finish their life without climbing the AGB. The corresponding (M ; Y_{ini}) domain of these so-called failed-AGB (see, e.g., [Greggio & Renzini 1990](#)) is shown in Fig. 15 (left of the No AGB/AGB line). These stars undergo central helium-burning at very high effective temperatures on the HB; there the stellar envelope surrounding the nuclear active core is extremely thin. Consequently, once helium fuel is exhausted at the center, the energy released by the contraction of the core and by hydrogen shell-burning mainly diffuses across the small, transparent helium-rich external layers and fails to swell them up. Therefore, the stars first evolve at constant effective temperature towards higher luminosity before moving directly towards the white dwarf region without passing through the AGB. This behavior has been proposed as a suitable explanation for the lack of sodium-rich stars on the AGB in NGC 6752 ([Charbonnel et al. 2013](#)). At 13.4 Gyr (and at 10 Gyr respectively), the models that are on the AGB have (M ; Y_{ini}) between (0.815; 0.248) and (0.67; 0.355) (respectively between (0.884; 0.248) and (0.599; 0.458)).

Nature of the white dwarfs: the composition (He vs. CO) of the stellar remnant strongly depends on the initial (M ; Y) as is shown in Fig. 15. In the case of canonical helium abundance no He-WDs are expected to be present in GCs today because the stellar lifetimes of the corresponding low-mass progenitors are much longer than the Hubble time⁸. However He-WDs are expected to form on much shorter lifetimes for increased initial helium abundance above ~ 0.33 ; in addition, the higher Y_{ini} , the lower the initial mass for the star to become a He-WD. The consequences of this behavior on the chemical properties of GC host WDs will be investigated in detail in a forthcoming paper.

6. Conclusions

This paper presents the first grid of models of low-mass stars (between 0.3 and $1 M_{\odot}$) with initial chemical composition derived from the ejecta of the fast rotating massive star models of [Decressin et al. \(2007a,b\)](#) at $[\text{Fe}/\text{H}] = -1.75$ mixed with original proto-GC gas. The initial helium mass fraction varies between 0.248 and 0.8, and the initial abundances of C, N, O, Na, Mg, and Al change accordingly.

The main properties of the models are presented as a function of initial mass and initial helium abundance. We discuss the effects of a very high initial helium content on the evolution paths in the HRD, on the duration and characteristics of the main evolutionary phases, and on the chemical nature of the WD remnants. We also give the predicted ranges in initial mass and helium content of the stars in different locations of the HRD at ages of 10 and 13.4 Gyr that delimit the age range of Galactic GCs.

This grid of models has been successfully used to explain the lack of Na-rich AGB stars in the GC NGC 6752 ([Charbonnel et al. 2014](#)). Other aspects related to the properties of stellar populations in GCs and of the GC CMDs at various phases of their evolution will be investigated in forthcoming papers in this series.

⁸ For $Y_{\text{ini}} = 0.248$ and $Z = 5 \times 10^{-4}$, the maximum initial mass of a He-WD progenitor is $0.738 M_{\odot}$, which has a turn-off age of ~ 17.6 Gyr. Therefore, for this composition He-WD might be expected only from exotic evolution paths; this can happen for example if the low-mass progenitors have undergone extreme mass-loss events, e.g., in close binary systems (e.g., [Webbink 1975](#); [Strickler et al. 2009](#)).

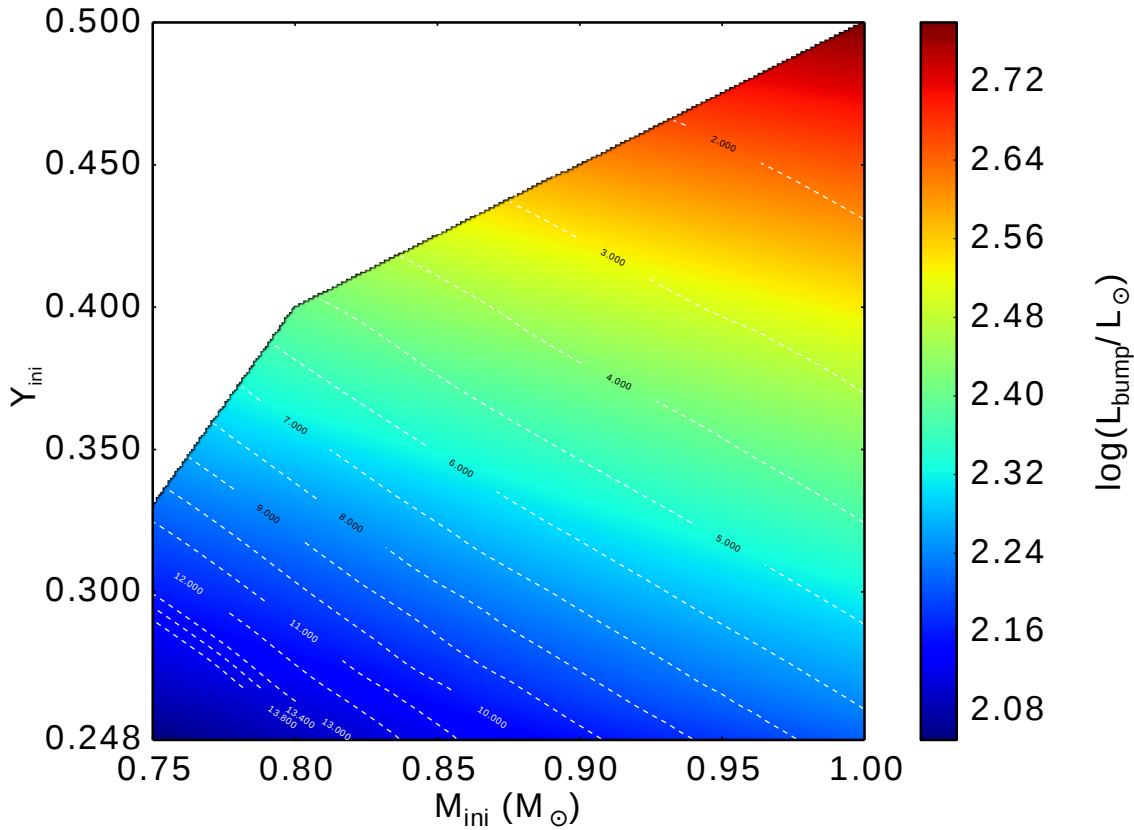


Fig. 14. Luminosity of the RGB bump as a function of initial stellar mass and Y_{ini} for those stars that undergo the bump before 14 Gyr (see ages given in Gyr along the dotted-line isochrones). The white area corresponds to the $(M; Y)$ domain where stars do not undergo the RGB bump (this is also the case for models with an initial mass lower than $0.75 M_{\odot}$).

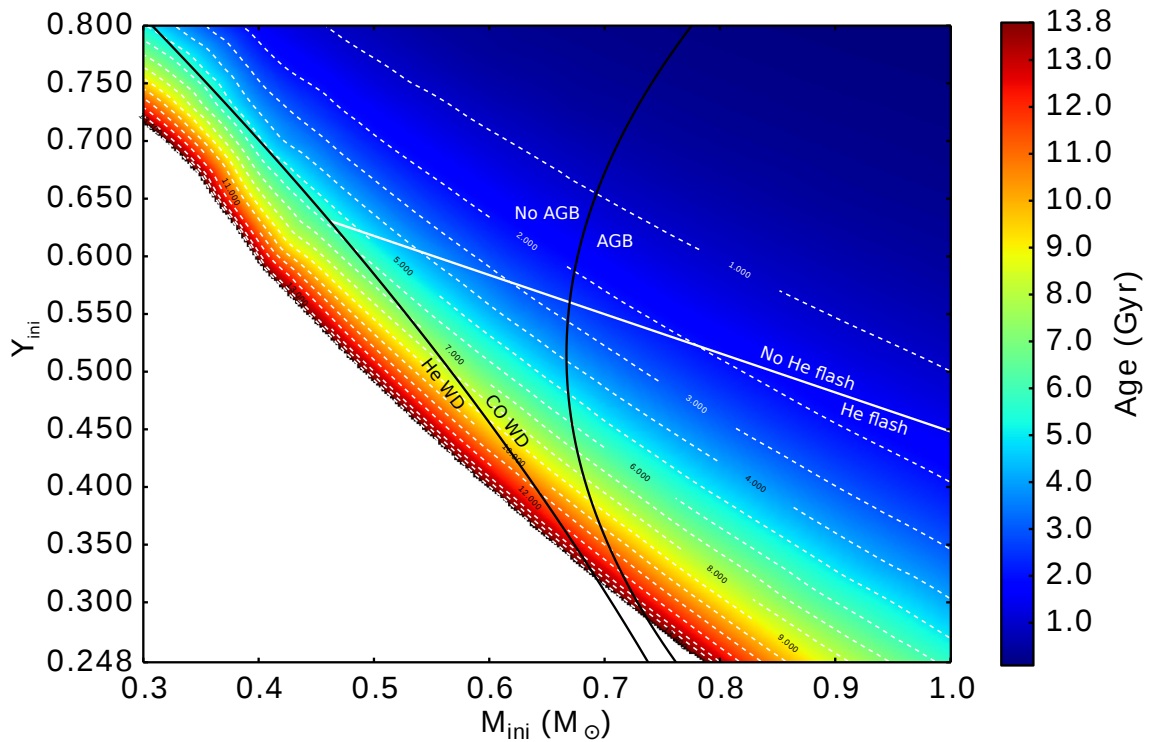


Fig. 15. Nature of the white dwarfs and failed-AGB phenomenon as a function of initial stellar mass and Y_{ini} . The black thin line on the left delimits the $(M; Y)$ domains where the stars become either He or CO white dwarfs; it crosses the white line that delimits the domains where helium ignition (when it occurs) starts with a flash or in non-degenerate conditions. The curved black thin line separates the stars that climb the AGB from those that do not (failed-AGB). Colors depict the age at the main sequence turn-off, with white dashed lines being isochrones with ages indicated in Gyr; the white area corresponds to the domain where stellar models predict main sequence lifetimes higher than 13.8 Gyr.

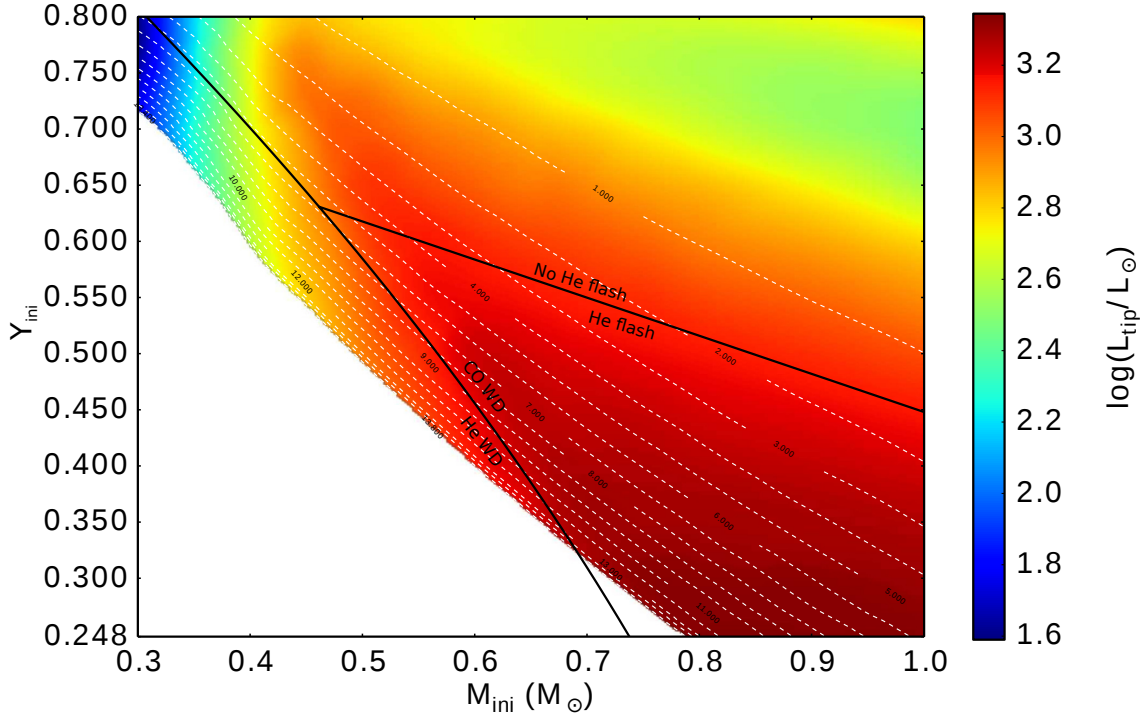


Fig. 16. Luminosity of the RGB tip (i.e., when helium ignition occurs) as a function of initial stellar mass and Y_{ini} . The black line delimits the domains where helium ignition (when it occurs) starts with a flash or in non-degenerate conditions. The colors indicate the luminosity of the RGB tip, with white dashed lines being isochrones with MS turn-off ages indicated in Gyr; the white area corresponds to the domain where stellar models predict main sequence lifetimes higher than 13.8 Gyr.

Acknowledgements. We thank G. Meynet for fruitful discussions and the anonymous referee for constructive suggestions on the manuscript. We acknowledge financial support from the Swiss National Science Foundation (FNS) for the project 200020-140346 “New perspectives on the chemical and dynamical evolution of globular clusters in light of new generation stellar models” (PI C.C.). We thank the International Space Science Institute (ISSI, Bern, CH) for welcoming the activities of ISSI Team 271 “Massive Star Clusters across the Hubble Time” (2013 – 2015; team leader C.C.). T.D. acknowledges financial support from the UE Programme (FP7/2007-2013) under grant No. 267251 “Astronomy Fellowships in Italy” (ASTROFit).

References

- Bastian, N., & Strader, J. 2014, *MNRAS*, **443**, 3594
- Bastian, N., Cabrera-Ziri, I., Davies, B., & Larsen, S. S. 2013a, *MNRAS*, **436**, 2852
- Bastian, N., Lamers, H. J. G. L. M., de Mink, S. E., et al. 2013b, *MNRAS*, **436**, 2398
- Bastian, N., Hollyhead, K., & Cabrera-Ziri, I. 2014, *MNRAS*, **445**, 378
- Bedin, L. R., Piotto, G., Anderson, J., et al. 2004, *ApJ*, **605**, L125
- Bragaglia, A., Sneden, C., Carretta, E., et al. 2014, *ApJ*, **796**, 68
- Cabrera-Ziri, I., Bastian, N., Davies, B., et al. 2014, *MNRAS*, **441**, 2754
- Caloi, V., & D’Antona, F. 2007, *A&A*, **463**, 949
- Campbell, S. W., D’Orazi, V., Yong, D., et al. 2013, *Nature*, **498**, 198
- Carretta, E. 2013, *A&A*, **557**, A128
- Carretta, E., Gratton, R. G., Lucatello, S., Bragaglia, A., & Bonifacio, P. 2005, *A&A*, **433**, 597
- Carretta, E., Bragaglia, A., Gratton, R. G., Lucatello, S., & Momany, Y. 2007, *A&A*, **464**, 927
- Carretta, E., Bragaglia, A., Gratton, R., D’Orazi, V., & Lucatello, S. 2009a, *A&A*, **508**, 695
- Carretta, E., Bragaglia, A., Gratton, R. G., et al. 2009b, *A&A*, **505**, 117
- Carretta, E., Bragaglia, A., Gratton, R. G., et al. 2010, *A&A*, **516**, A55
- Carretta, E., Bragaglia, A., Gratton, R. G., Lucatello, S., & D’Orazi, V. 2012, *ApJ*, **750**, L14
- Cassisi, S., & Salaris, M. 2014, *A&A*, **563**, A10
- Cassisi, S., Mucciarelli, A., Pietrinferni, A., Salaris, M., & Ferguson, J. 2013, *A&A*, **554**, A19
- Charbonnel, C., Chantreau, W., Decressin, T., Meynet, G., & Schaerer, D. 2013, *A&A*, **557**, L17
- Charbonnel, C., Chantreau, W., Krause, M., Primas, F., & Wang, Y. 2014, *A&A*, **569**, L6
- Coc, A., Uzan, J.-P., & Vangioni, E. 2013, ArXiv e-prints [arXiv:1307.6955]
- Dallessandro, E., Salaris, M., Ferraro, F. R., et al. 2011, *MNRAS*, **410**, 694
- D’Antona, F., & Caloi, V. 2004, *ApJ*, **611**, 871
- D’Antona, F., Caloi, V., Montalbán, J., Ventura, P., & Gratton, R. 2002, *A&A*, **395**, 69
- D’Antona, F., Bellazzini, M., Caloi, V., et al. 2005, *ApJ*, **631**, 868
- D’Antona, F., Caloi, V., & Ventura, P. 2010, *MNRAS*, **405**, 2295
- D’Antona, F., Ventura, P., Decressin, T., Vesperini, E., & D’Ercole, A. 2014, *MNRAS*, **443**, 3302
- de Mink, S. E., Pols, O. R., Langer, N., & Izzard, R. G. 2009, *A&A*, **507**, L1
- Decressin, T., Charbonnel, C., & Meynet, G. 2007a, *A&A*, **475**, 859
- Decressin, T., Meynet, G., Charbonnel, C., Prantzos, N., & Ekström, S. 2007b, *A&A*, **464**, 1029
- Demarque, P., Mengel, J. G., & Aizenman, M. L. 1971, *ApJ*, **163**, 37
- Denissenkov, P. A., & Hartwick, F. D. A. 2014, *MNRAS*, **437**, L21
- D’Ercole, A., D’Antona, F., Ventura, P., Vesperini, E., & McMillan, S. L. W. 2010, *MNRAS*, **407**, 854
- D’Ercole, A., D’Antona, F., & Vesperini, E. 2011, *MNRAS*, **415**, 1304
- D’Ercole, A., D’Antona, F., Carini, R., Vesperini, E., & Ventura, P. 2012, *MNRAS*, **423**, 1521
- Doherty, C. L., Gil-Pons, P., Lau, H. H. B., Lattanzio, J. C., & Siess, L. 2014, *MNRAS*, **437**, 195
- Dotter, A., Sarajedini, A., Anderson, J., et al. 2010, *ApJ*, **708**, 698
- Forestini, M., & Charbonnel, C. 1997, *A&AS*, **123**, 241
- Gratton, R. G., Carretta, E., Bragaglia, A., Lucatello, S., & D’Orazi, V. 2010, *A&A*, **517**, A81
- Greggio, L., & Renzini, A. 1990, *ApJ*, **364**, 35
- Grevesse, N., & Noels, A. 1993, in *Origin and Evolution of the Elements*, eds. N. Prantzos, E. Vangioni-Flam, & M. Casse, 15
- Iben, I., & Rood, R. T. 1969, *Nature*, **223**, 933
- Iben, Jr., I., & Faulkner, J. 1968, *ApJ*, **153**, 101
- Izzard, R. G., de Mink, S. E., Pols, O. R., et al. 2013, *Mem. Soc. Astron. It.*, **84**, 171
- King, I. R., Bedin, L. R., Cassisi, S., et al. 2012, *AJ*, **144**, 5
- Kippenhahn, R., Weigert, A., & Weiss, A. 2013, *Stellar Structure and Evolution* (Springer)
- Krause, M., Charbonnel, C., Decressin, T., Meynet, G., & Prantzos, N. 2013, *A&A*, **552**, A121

- Kruijssen, J. M. D. 2014, *Class. Quant. Grav.*, **31**, 244006
- Lagarde, N., Decressin, T., Charbonnel, C., et al. 2012, *A&A*, **543**, A108
- MacLean, B. T., De Silva, G. M., & Lattanzio, J. 2015, *MNRAS*, **446**, 3556
- Maeder, A. 2009, *Physics, Formation and Evolution of Rotating Stars* (Berlin, Heidelberg: Springer)
- Maeder, A., & Meynet, G. 2006, *A&A*, **448**, L37
- Marino, A. F., Milone, A. P., Przybilla, N., et al. 2014, *MNRAS*, **437**, 1609
- Martell, S. L., & Grebel, E. K. 2010, *A&A*, **519**, A14
- Milone, A. P., Bedin, L. R., Piotto, G., et al. 2008, *ApJ*, **673**, 241
- Milone, A. P., Piotto, G., King, I. R., et al. 2010, *ApJ*, **709**, 1183
- Milone, A. P., Marino, A. F., Piotto, G., et al. 2013, *ApJ*, **767**, 120
- Mowlavi, N., Meynet, G., Maeder, A., Schaerer, D., & Charbonnel, C. 1998, *A&A*, **335**, 573
- Palacios, A., Charbonnel, C., Talon, S., & Siess, L. 2006, *A&A*, **453**, 261
- Pasquini, L., Bonifacio, P., Molaro, P., et al. 2005, *A&A*, **441**, 549
- Pietrinferni, A., Cassisi, S., Salaris, M., Percival, S., & Ferguson, J. W. 2009, *ApJ*, **697**, 275
- Piotto, G. 2008, *Mem. Soc. Astron. It.*, **79**, 334
- Piotto, G. 2009, in *IAU Symp. 258*, eds. E. E. Mamajek, D. R. Soderblom, & R. F. G. Wyse, 233
- Piotto, G., Bedin, L. R., Anderson, J., et al. 2007, *ApJ*, **661**, L53
- Planck Collaboration XVI 2014, *A&A*, **571**, A16
- Prantzos, N., & Charbonnel, C. 2006, *A&A*, **458**, 135
- Prantzos, N., Charbonnel, C., & Iliadis, C. 2007, *A&A*, **470**, 179
- Ramírez, I., Meléndez, J., & Chanamé, J. 2012, *ApJ*, **757**, 164
- Reimers, D. 1975, *Mem. Soc. Roy. Sci. Liège*, **8**, 369
- Salaris, M., & Cassisi, S. 2005, *Evolution of Stars and Stellar Populations* (Wiley-VCH), 400
- Salaris, M., & Cassisi, S. 2014, *A&A*, **566**, A109
- Sbordone, L., Salaris, M., Weiss, A., & Cassisi, S. 2011, *A&A*, **534**, A9
- Siess, L. 2007, *A&A*, **476**, 893
- Sills, A., & Glebbeek, E. 2010, *MNRAS*, **407**, 277
- Strickler, R. R., Cool, A. M., Anderson, J., et al. 2009, *ApJ*, **699**, 40
- Sweigart, A. V. 1978, in *The HR Diagram – The 100th Anniversary of Henry Norris Russell*, eds. A. G. D. Philip, & D. S. Hayes, *IAU Symp.*, **80**, 333
- Valcarce, A. A. R., Catelan, M., & Sweigart, A. V. 2012, *A&A*, **547**, A5
- Vassiliadis, E., & Wood, P. R. 1993, *ApJ*, **413**, 641
- Ventura, P., & D’Antona, F. 2011, *MNRAS*, **410**, 2760
- Ventura, P., D’Antona, F., Mazzitelli, I., & Gratton, R. 2001, *ApJ*, **550**, L65
- Ventura, P., Di Criscienzo, M., Carini, R., & D’Antona, F. 2013, *MNRAS*, **431**, 3642
- Villanova, S., Piotto, G., King, I. R., et al. 2007, *ApJ*, **663**, 296
- Villanova, S., Piotto, G., & Gratton, R. G. 2009, *A&A*, **499**, 755
- Webbink, R. F. 1975, *MNRAS*, **171**, 555

Appendix A: Content of electronic tables for the grid

Table A.1. Description of table containing the results of our evolution models.

Stellar parameters	Surface abundances	Central abundances
– Model number	$^1\text{H } ^2\text{H}$	^1H
– Maximum temperature T_{max} (K)	$^3\text{He } ^4\text{He}$	$^3\text{He } ^4\text{He}$
– Mass coordinate of T_{max} (M_{\odot})	$^6\text{Li } ^7\text{Li}$	
– Effective temperature T_{eff} (K)	$^7\text{Be } ^9\text{Be}$	
– Surface luminosity L (L_{\odot})	$^{10}\text{B } ^{11}\text{B}$	
– Photospheric radius R_{eff} (R_{\odot})	$^{12}\text{C } ^{13}\text{C } ^{14}\text{C}$	$^{12}\text{C } ^{13}\text{C } ^{14}\text{C}$
– Photospheric density ρ_{eff} (g cm^{-3})	$^{14}\text{N } ^{15}\text{N}$	^{14}N
– Density at the location of T_{max} , ρ_{max} (g cm^{-3})	$^{16}\text{O } ^{17}\text{O } ^{18}\text{O}$	$^{16}\text{O } ^{17}\text{O } ^{18}\text{O}$
– Stellar mass M (M_{\odot})	^{19}F	^{19}F
– Mass-loss rate ($M_{\odot} \text{ yr}^{-1}$)	$^{20}\text{Ne } ^{21}\text{Ne } ^{22}\text{Ne}$	$^{20}\text{Ne } ^{21}\text{Ne } ^{22}\text{Ne}$
– Age t (yr)	^{23}Na	^{23}Na
– Photospheric gravity $\log(g_{\text{eff}})$ ($\log(\text{cgs})$)	$^{24}\text{Mg } ^{25}\text{Mg } ^{26}\text{Mg}$	$^{24}\text{Mg } ^{25}\text{Mg } ^{26}\text{Mg}$
– Central temperature T_{c} (K)	$^{26}\text{Al } ^{27}\text{Al}$	$^{26}\text{Al } ^{27}\text{Al}$
– Central pressure P_{c}	^{28}Si	^{28}Si
– Mass at the base of convective envelope (M_{\odot})		
– Mass of the core (M_{\odot})		

We provide files containing relevant evolution characteristics (Table A.1) for the 224 models of the present grid⁹. For each mass and initial helium content, models predictions are provided from the beginning of the pre-main sequence (along the Hayashi track) up to the brightest point of the evolution on the AGB. For each model, we have selected 500 points to allow a good description of the full raw tracks. First, the most important evolution keypoints are determined:

1. the beginning of the pre-main sequence;
2. the zero age main-sequence defined as the time when the central hydrogen abundance has decreased by 0.003 in mass fraction compared to its initial value.
3. the turning point when the central mass fraction of hydrogen is equal to 0.06 on the main sequence;
4. the end of core H-burning
5. the bottom of the red giant branch (RGB);
6. the RGB-tip;
7. the local minimum of luminosity during central He-burning;
8. the local maximum of T_{eff} during central He-burning;
9. the bottom of AGB: the point with the local minimum of luminosity after the loop on HB;

10. the brightest point on the AGB.

Then, we chose points from the results of evolutionary computation as follows:

- 100 points are determined alongside the pre-main sequence with constant time-steps. The value of each quantity given in Table A.1 is computed from their values taken from the two nearest models calculated with STAREVOL.
- The same procedure is applied between points 2 and 3 and points 3 and 4 where we use step in X_{C} instead of time; 85 and 25 points are selected, respectively.
- Between keypoints 4 and 5 we interpolate 60 points with equal time steps.
- Then 20 points are determined between keypoints 5 and 6 with equal intervals of $\log L$.
- 20, 70, and 70 points are selected with equal central helium abundance Y_{C} steps between keypoints 6 and 7, keypoints 7 and 8, and keypoints 8 and 9.
- 50 points are selected between keypoints 9 and 10 with the same $\log L$ step on the AGB.

⁹ All data detailed in Table A.1 are available at the CDS and on the website <http://obswww.unige.ch/Recherche/evol/-Database>